Nano Research

Open Access

Research Article

Synthesis of NiMo–$NiMoO_x$ with crystalline/amorphous heterointerface for enhanced hydrogen evolution reaction

Xinjia Tan[1], Zhong Wang[1], Jiaqi Liu[1,2], Jinshuo Yang[1], Qiang Wang[2] ✉, and Shuang Yuan[1,3] ✉

[1] *School of Metallurgy, Northeastern University, Shenyang 110819, China*
[2] *Key Laboratory of Electromagnetic Processing of Materials (Ministry of Education), Northeastern University, Shenyang 110819, China*
[3] *Key Laboratory for Ecological Metallurgy of Multimetallic Mineral (Ministry of Education), Northeastern University, Shenyang 110819, China*

Cite this article: *Nano Research*, **2025**, *18*, 94907368. https://doi.org/10.26599/NR.2025.94907368

ABSTRACT: Constructing crystalline-amorphous heterostructure has been verified as an efficient strategy for boosting the activity of metal/oxides-based electrocatalysts in alkaline hydrogen evolution reaction (HER). Crystalline metal possesses high electronic conductivity, while amorphous structure provides numerous active sites. Herein, the crystalline-amorphous NiMo–$NiMoO_x$ electrocatalyst was fabricated by a facile electrodeposition approach, and the introduction of Mo atoms can effectively modulate the interface between crystalline and amorphous regions as well as the electron structure of active sites. Benefiting from the synergistic interaction of the crystalline-amorphous heterostructure and the introduction of Mo atoms, the NiMo–$NiMoO_x$ electrocatalyst exhibits remarkable HER catalytic properties and durability. It requires a low overpotential of 30 mV at the current density of 10 mA·cm^{-2} in 1.0 M KOH, as well as a long-term stability with slight degradation after operating for over 80 h. Moreover, it also exhibits excellent activity and stability with negligible declination in the simulated alkaline seawater, making it highly promising for seawater electrolysis applications. Density functional theory (DFT) calculations demonstrate the electron distribution at the interface reduces the energy barrier for the water dissociation and optimizes H adsorption/desorption capability, thereby enhancing HER kinetics. This work provides a feasible strategy for designing high-efficiency, low-cost HER electrocatalysts based on crystalline-amorphous heterostructures.

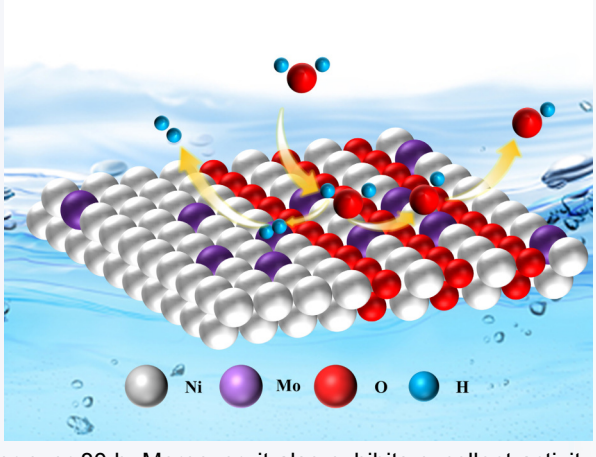

KEYWORDS: crystalline-amorphous heterostructure, synergistic effect, electrodeposition, seawater, hydrogen evolution reaction (HER)

1 Introduction

Hydrogen (H_2) is regarded as a renewable and eco-friendly energy source, which is promising for substituting fossil fuels and alleviating the pressure of the energy crisis and environmental issues [1–4]. Besides, hydrogen can be used in many fields as a kind of high-value product, including medicine, chemical industry, agriculture, and others. Alkaline water splitting has the advantages of low cost, long lifetime, and ease of maintenance and is widely applied commercially [5–7]. In addition, seawater can be utilized to produce hydrogen, along with abundant solar and wind energy near the coastline, thus reducing the cost of hydrogen production. However, the sluggish kinetics of hydrogen evolution reaction (HER) inhibit the further development of alkaline water splitting [8]. Though noble-metal catalysts can greatly boost the HER process, they are difficult to meet the requirements of industrial production due to the high price and scarcity [9, 10]. Thus, it is urgent to develop low-cost and highly efficient catalysts for alkaline water splitting.

Among non-precious metal-based catalysts, Ni–NiO catalysts have attracted much attention because Ni metal is abundant in the earth and inexpensive [11–13]. Besides, Ni–NiO catalysts exhibit excellent electrocatalytic activity due to the synergistic effect [14–16].

Received: January 11, 2025; **Revised:** February 28, 2025
Accepted: March 14, 2025

✉Address correspondence to Shuang Yuan, yuans@smm.neu.edu.cn; Qiang Wang, wangq@mail.neu.edu.cn

Many studies have demonstrated that NiO can promote the dissociation of water molecules and accelerate the Volmer step, while Ni can provide active sites for the adsorption/desorption of hydrogen intermediates and facilitate the Heyrovsky/Tafel step. Several strategies have been employed to improve the activity of Ni–NiO catalysts through modulating the d-band center. For example, Zhao et al. found that the ratio of Ni to NiO can significantly enhance alkaline HER activity [17]. Yan et al. constructed few-layered carbon on Ni–NiO to enhance the activity and stability of the catalyst [18]. However, the activity of Ni–NiO catalysts is still far away from that of noble catalysts.

Recently, phase and interface engineering via crystalline-amorphous heterostructures has become an attractive strategy for fabricating highly active HER electrocatalysts due to the synergistic effect and intriguing phase properties [19, 20]. Compared to the crystalline phase, the amorphous phase exhibits a distinctively disordered atomic arrangement with abundant defects and unsaturated coordination environments, providing more active sites [21–24]. In addition, the isotropic and flexible properties of the amorphous phase enable an easily adjustable local electronic structure at the active sites, which can optimize the intermediates' adsorption/dissociation capability [25–27]. Moreover, the amorphous phase can also enhance the wettability of the catalysts, facilitating the mass transfer and bubble release [28, 29]. The crystalline phase, on the other hand, possesses high electrical conductivity and lower metal ion leaching. Thus, the integration of the crystalline phase with the amorphous phase can improve the electrical conductivity and stability of the catalysts, which are the shortcomings of the amorphous phase [30–32]. Although the crystalline-amorphous heterostructures for HER have been studied to some extent, there are still few studies focusing on modulating the interface of the heterostructure by incorporating other atoms, such as Mo atoms.

Inspired by the above considerations, we synthesized the crystalline-amorphous NiMo–NiMoO$_x$ heterostructure and demonstrated the structure–activity relationship between the crystalline and amorphous phases. The experimental results proved that the introduction of Mo atoms could effectively decrease the ratio of crystalline to amorphous areas, resulting in abundant interfaces and active sites. Besides, X-ray absorption spectroscopy (XAS) results and density functional theory (DFT) calculations confirmed that there was electron redistribution between Mo and Ni atoms, contributing to the optimized electronic structure. As a result, NiMo–NiMoO$_x$ exhibited a lower energy barrier for water dissociation ($\Delta G_{H_2O^*}$ = 0.134 eV) and an optimized capacity for hydrogen adsorption/desorption (ΔG_{H^*} = 0.240 eV), compared to Ni–NiO$_x$ (0.736 eV for water dissociation and 0.547 eV for hydrogen adsorption/desorption, respectively). Thus, NiMo–NiMoO$_x$ only requires 30 mV to deliver the current density of 10 mA·cm^{-2} and can operate for 80 h with only slight decay. Besides, it can also perform well in the simulated alkaline seawater for 96 h, showing promise for the alkaline seawater splitting.

2 Experimental

NiMo–NiMoO$_x$ catalyst was prepared by electrodeposition on the commercial Ni foam at 50 °C with a slow stirring rate of 300 rpm. The Ni foam was ultrasonically cleaned in ethanol, diluted HCl, and then deionized water for 10 min prior to use. For the electrodeposition of NiMo–NiMoO$_x$ catalyst, $NiCl_2{\cdot}6H_2O$ and Na_2MoO_4 were used as the metal sources and $K_4P_2O_7$, $C_2H_5NO_2$, and $CO(NH_2)_2$ were added to the deposition solution as additional agents. The electrolyte contained 0.6 M $K_4P_2O_7$, 0.3 M $C_2H_5NO_2$, 1 M $CO(NH_2)_2$, 0.25 M $NiCl_2{\cdot}6H_2O$, and 0.01 M Na_2MoO_4. The NiMo–NiMoO$_x$ catalyst was prepared with two electrode electrodeposition at 200 mA·cm^{-2} for 20 min. The synthesis of Ni–NiO$_x$ was similar to NiMo–NiMoO$_x$, except that the solution was prepared without Na_2MoO_4. The material characterizations and electrochemical measurements are displayed in the Electronic Supplementary Material (ESM).

3 Results and discussion

We first studied the adsorption ability of H and H_2O on Ni–NiO$_x$ and NiMo–NiMoO$_x$ through DFT calculations. As shown in Fig. 1(a), the structure of Ni–NiO$_x$ consists of the crystalline Ni (111) and the amorphous NiO$_x$. Because the amorphous structure possesses short-range order, it exhibits similar properties to the crystalline structure within a small region of only a few atomic layers. In this study, crystalline NiO was utilized as a model for amorphous NiO$_x$ and was further optimized to obtain a relatively stable structure. By replacing some Ni atoms with Mo atoms, we also successfully fabricated the structure of NiMo–NiMoO$_x$. To initially investigate the HER process on Ni–NiO$_x$, we selected some Ni atoms as the active sites, as shown in Fig. S1(a) in the ESM. The calculation results are presented in Table S1 in the ESM.

The H_2O adsorption energy value obtained on the Ni1 site is −2.04 eV, which is much lower than that of other Ni sites. This suggests that H_2O prefers to adsorb on the Ni1 site. Besides, the H-binding energy value on the Ni3 site is the lowest (−1.38 eV), indicating that H atoms are more likely to adsorb on the Ni3 site. According to the calculation results, it can be speculated that H_2O molecules first adsorb on the Ni1 site and split into H and OH. Subsequently, H tends to adsorb on the Ni1 site, while OH is released from the surface. From the calculation results, it is worth noting that the HER process prefers to occur at the interface between the crystalline Ni and amorphous NiO$_x$ due to the decreased adsorption energy of H_2O and H with increasing distance from the interface. The adsorption energies of H_2O and H in NiMo–NiMoO$_x$ were then calculated, and the active sites and relevant adsorption energies are shown in Fig. S1(b) and Table S2 in the ESM. It is clearly shown that the incorporation of Mo atoms into Ni–NiO$_x$ efficiently regulates the adsorption energies of both H_2O and H in Fig. 1(b). H_2O molecules first adsorb on the Mo2 site and split into H and OH. The absorption energy value of H_2O on the Mo2 site is −1.22 eV, which is much smaller than that in Ni–NiO$_x$, greatly decreasing the energy barrier for water dissociation. Additionally, the H adsorption energy on the Ni3 site is only −0.75 eV, much closer to the optimal value for H_2 evolution. The detailed HER process is illustrated in Fig. 1(c). The above theoretical results demonstrate that the incorporation of Mo atoms in metallic Ni and bimetallic oxide NiMoO$_x$ can modulate the intrinsic interactions with H_2O and H involved in the alkaline HER process. Thus, rational control of the Mo content is expected to enable efficient water dissociation and facile H_2 evolution, leading to improved performance in alkaline HER.

As illustrated in Fig. 2(a), the NiMo–NiMoO$_x$ crystalline-amorphous heterostructure is directly grown on Ni foam through a facile one-step electrodeposition strategy [33, 34]. The detailed crystallinity and phase information of Ni–NiO$_x$ and

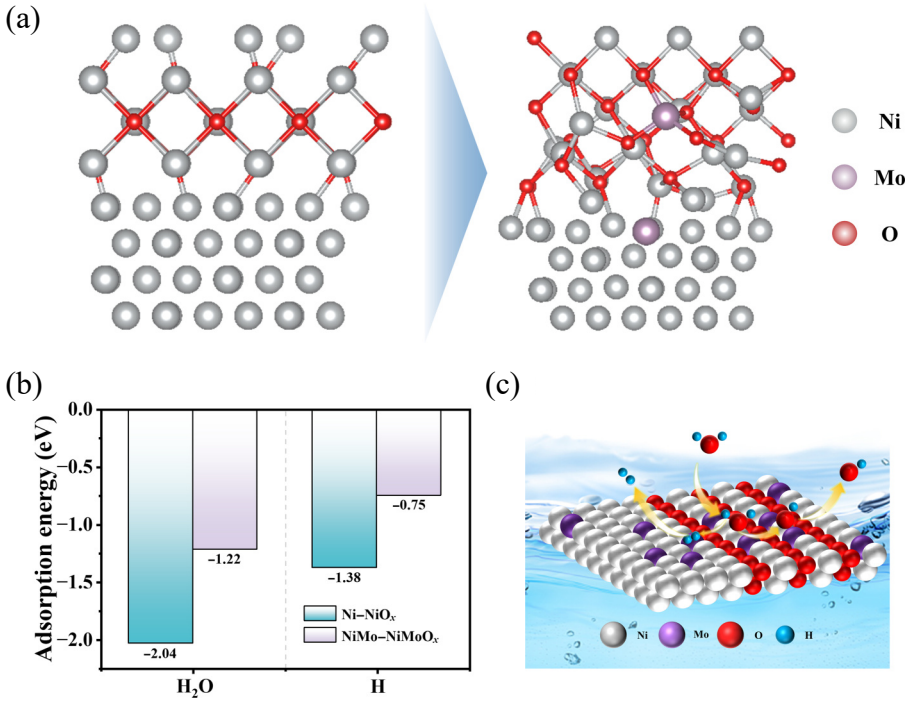

Figure 1 (a) Models of Ni–NiO_x and NiMo–$NiMoO_x$. (b) Calculated H_2O and H adsorption energies of Ni–NiO_x and NiMo–$NiMoO_x$. (c) Predicted HER process of NiMo–$NiMoO_x$.

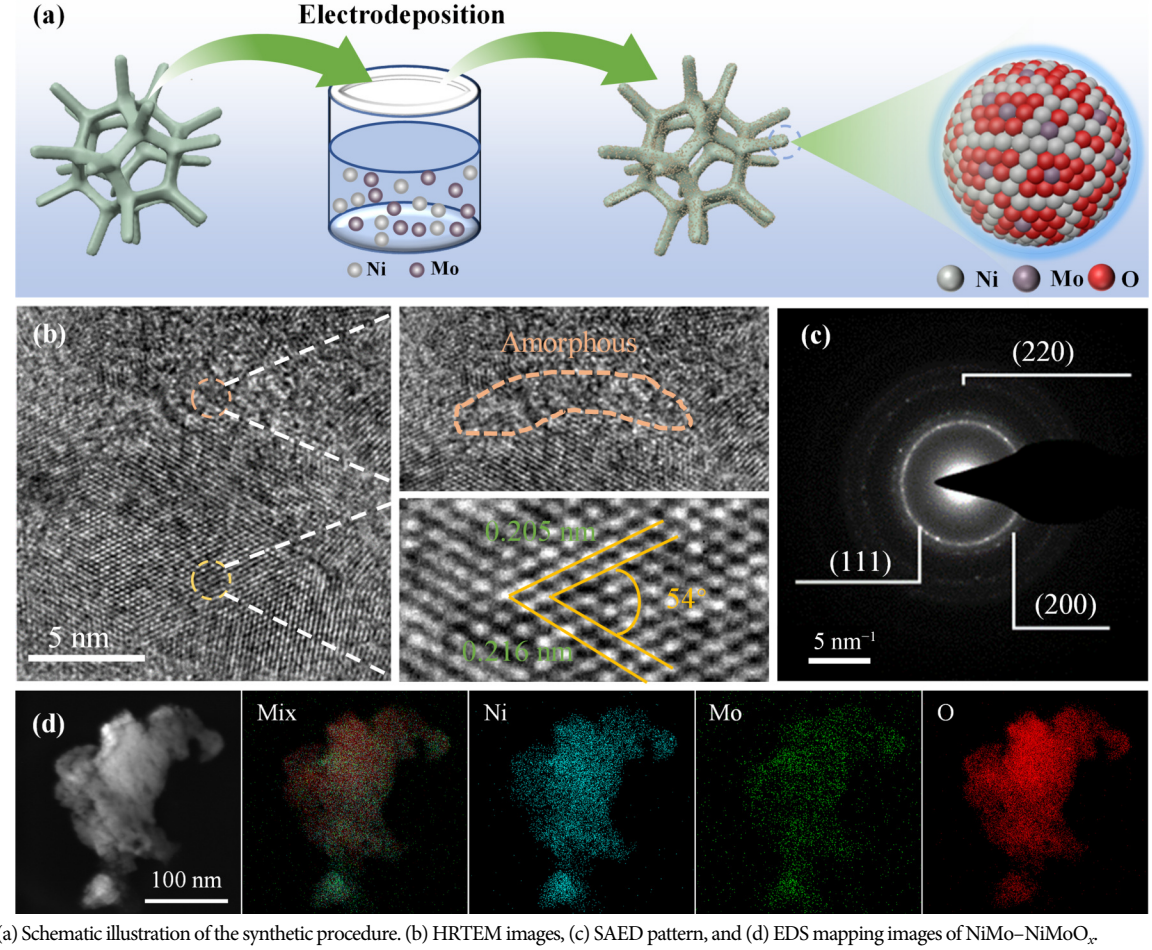

Figure 2 (a) Schematic illustration of the synthetic procedure. (b) HRTEM images, (c) SAED pattern, and (d) EDS mapping images of NiMo–$NiMoO_x$.

NiMo–NiMoO$_x$ were characterized using X-ray diffraction (XRD) measurement. Due to the strong interference of Ni peaks originating from the Ni foam, carbon paper was chosen as the substrate to investigate the crystal information of the samples. Figure S2 in the ESM shows that the XRD patterns for all samples feature a major diffraction peak at about 26°, which can be assigned to the carbon paper substrate [35]. The Ni–NiO$_x$ and NiMo–NiMoO$_x$ exhibit three major diffraction peaks at about 44.5°, 51.8°, and 76.4°, which could be indexed to the (111), (200), and (220) planes of Ni (PDF # 04-0850) [18, 36]. Moreover, no typical diffraction peaks related to Ni(Mo)O$_x$ are observed. Compared to the peaks of Ni–NiO$_x$, relatively broadened, lower intensity, and shifted diffraction peaks could be observed clearly after the introduction of Mo source to the bath, suggesting that NiMo–NiMoO$_x$ possesses a smaller particle size and grain refinement [34, 37, 38]. Considering the above analysis, it can be inferred that Mo source in the bath can effectively modulate the formation of the NiMo–NiMoO$_x$ in the electrodeposition process and may increase the interfaces between the crystalline and amorphous phases.

It has been verified that a hydrophilic structure can facilitate mass transport and bubble release from the electrode surface, thus accelerating the HER process [39, 40]. As shown in Fig. S3 in the ESM, the contact angles between water and the samples are measured to be zero almost instantly when water is dropped onto the surface, while the process on NiMo–NiMoO$_x$ is faster than that on Ni–NiO$_x$. NiMo–NiMoO$_x$ needed only 8 ms to be completely infiltrated, while Ni–NiO$_x$ needed 66 ms. According to previous studies, Ni foam exhibits poor hydrophilicity, with a contact angle reaching 126° [41, 42]. The results indicate that the as-fabricated catalysts have excellent hydrophilicity, and the introduction of Mo atoms likely plays a key role in enhancing the hydrophilicity of NiMo–NiMoO$_x$. Figure S4 in the ESM displays the scanning electron microscopy (SEM) images of the NiMo–NiMoO$_x$ catalyst along with the NF and Ni–NiO$_x$. As shown in the images, a dense film was formed on the surface of Ni foam after electrodeposition. The high-magnification images show that Ni–NiO$_x$ consists of irregular nanoparticles with a diameter of about 70 nm, uniformly distributed on the surface. In contrast, the nanoparticle size of NiMo–NiMoO$_x$ is smaller, indicating that the introduction of Mo atoms can also affect the morphology of Ni–NiO$_x$.

In Fig. 2(b), the detailed high-resolution transmission electron microscopy (HRTEM) images reveal that NiMo–NiMoO$_x$ consists of both amorphous and crystal phases. As shown in the enlarged views of crystal regions, the interplanar spacings of the lattice fringes are precisely measured to be 0.205 and 0.216 nm with the interplanar angle of 54°. These spacings correspond to the (200) and (111) planes of Ni, respectively. The enlarged interplanar spacings may be attributed to the incorporation of Mo atoms into the Ni crystal lattice. In addition, numerous regions lacking lattice fringes confirm the presence of amorphous NiMoO$_x$ between well-crystallized NiMo nanoparticles. The selected area electron diffraction (SAED) pattern of NiMo–NiMoO$_x$, shown in Fig. 2(c), further corroborates the coexistence of amorphous NiMoO$_x$ and crystalline Ni. Moreover, energy dispersive spectroscopy (EDS) mapping images in Fig. 2(d) indicate that Ni, Mo, and O are uniformly distributed throughout the whole area. The element ratios and inductively coupled plasma (ICP) results of NiMo–NiMoO$_x$, presented in Fig. S5 in the ESM, further confirm the existence of NiMoO$_x$. Collectively, these results demonstrate the successful synthesis of the crystalline-amorphous NiMo–NiMoO$_x$ heterostructure.

The surface electronic structure of NiMo–NiMoO$_x$ was investigated and compared with that of Ni–NiO$_x$ by X-ray photoelectron spectroscopy (XPS) measurement. As shown in Fig. S6 in the ESM, there are obvious Ni, Mo, and O peaks in the XPS spectra of NiMo–NiMoO$_x$, confirming the presence of these elements. As revealed by Ni 2p XPS spectra of NiMo–NiMoO$_x$ (Fig. 3(b)) and Ni–NiO$_x$ (Fig. S7(a) in the ESM), the surface of both samples is in a metallic state with partial oxidation. The Mo 3d XPS spectrum (Fig. 3(a)) shows the coexistence of metallic Mo atoms and oxidized Mo atoms [43–45]. Notably, the binding energy of Ni 2p in NiMo–NiMoO$_x$ exhibits a negative shift of 0.2 eV compared to Ni–NiO$_x$, suggesting that Ni in NiMo–NiMoO$_x$ is electron-rich, likely due to the electron transfer between Ni and Mo atoms. The O 1s spectra of both samples (Fig. 3(c) and Fig. S7(b) in the ESM) are deconvoluted to the Metal–O bond, oxygen vacancies, and hydroxyl group [45–47].

The comprehensive characterizations and analyses presented in the manuscript conclusively demonstrate that the NiMo–NiMoO$_x$ composite system comprises both crystalline NiMo alloys and amorphous NiMoO$_x$ oxides. Notably, XPS measurement reveals that the proportion of Ni^0 and Ni^{2+} species can serve as a reliable quantitative indicator of the crystalline-amorphous ratio. To systematically investigate the influence of Mo content on the crystalline-amorphous ratio, XPS measurements were performed on samples with varying Mo concentrations in the bath. As shown in Fig. S8 and Table S3 in the ESM, the Ni^0/Ni^{2+} ratio progressively decreases from 49:51 to 7:93 with increasing Mo content. It suggests that higher Mo concentrations significantly promote the formation of the amorphous phase, thereby modulating the proportions of crystalline and amorphous phase. Additionally, compared with the Ni 2p spectrum of Ni–NiO$_x$, the binding energies of Ni 2p in NiMo–NiMoO$_x$ shifted negatively with varying Mo content, suggesting the electron transfer from Mo atoms to Ni atoms. Moreover, the binding energies of Ni 2p in NiMo–NiMoO$_x$ remain relatively constant with different Mo content, likely due to the stable Mo content in the NiMo alloys.

To further investigate the electronic states and atomic structures, synchrotron radiation-based X-ray absorption fine structure (XAFS) spectroscopy was performed on NiMo–NiMoO$_x$ with standard samples (Ni foil and NiO) as references. Figure 3(d) shows the Ni K-edge X-ray absorption near-edge structure (XANES) spectra of NiMo–NiMoO$_x$, Ni foil, and NiO. The absorption energy (E_0) of Ni in NiMo–NiMoO$_x$ is lower than that in the NiO while higher than that in the Ni foil. It indicates that Ni in NiMo–NiMoO$_x$ exists in both metallic and oxide states, which is in accordance with the XPS results [48, 49]. The Fourier transformed (FT) Ni K-edge extended XAFS (EXAFS) spectra (Fig. 3(e)) were analyzed to investigate the local structure of Ni atoms. The Ni foil exhibits a dominant Ni–Ni peak at 2.48 Å, while NiO shows a Ni–O peak at 2.08 Å. For NiMo–NiMoO$_x$, a strong peak at 2.51 Å can be attributed to Ni–M (Ni/Mo) bond and the band length increases compared to Ni foil, likely due to the incorporation of Mo atoms [50, 51]. Besides, the intensity of Ni–Ni peak in the NiMo–NiMoO$_x$ is lower than that in the Ni foil, possibly due to a decreased coordination number. The fitting results (Fig. S9 and Table S4 in the ESM) further demonstrate the bonding information, showing a strong Ni–Ni peak and a minor Ni–O peak for NiMo–NiMoO$_x$. Though in the small wavelet transform (WT)

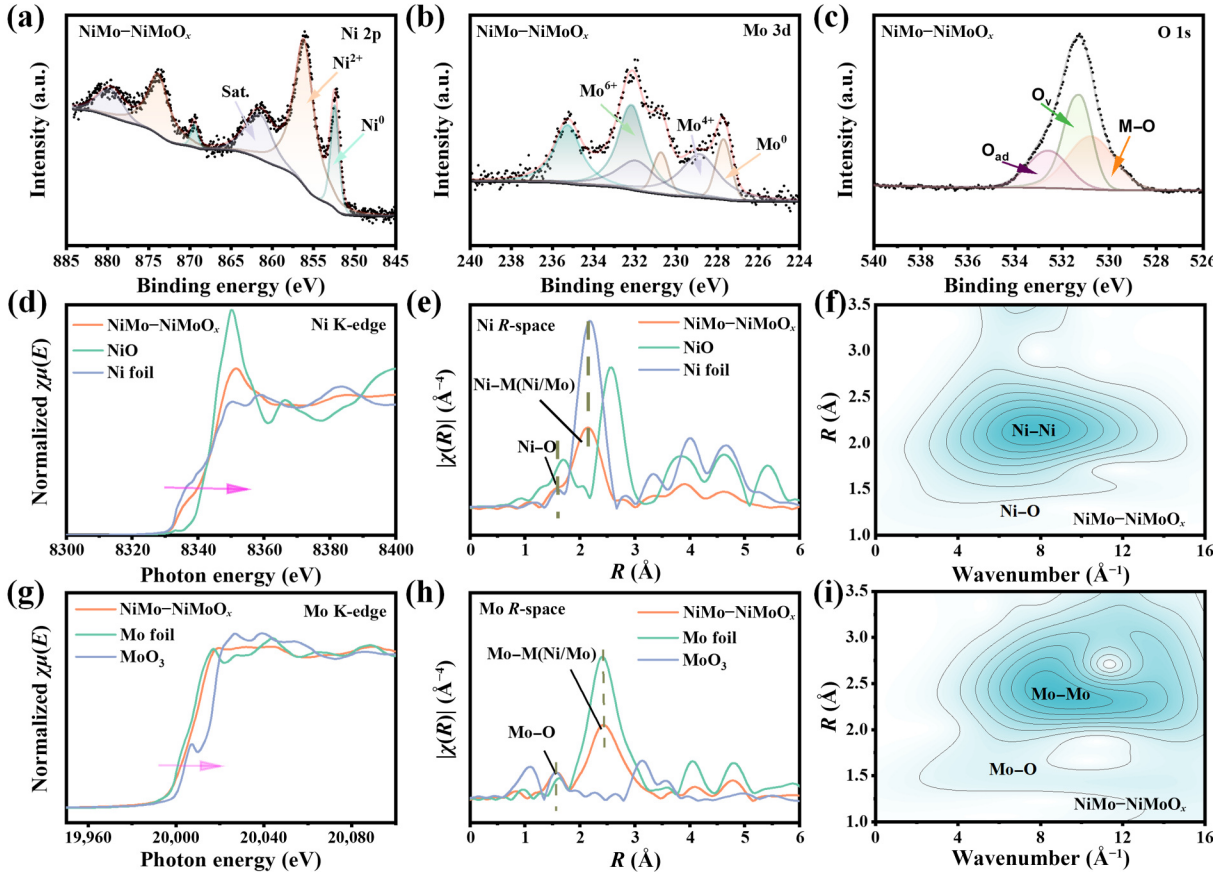

Figure 3 XPS spectra of (a) high-resolution Ni 2p, (b) high-resolution Mo 3d, and (c) high-resolution O 1s for NiMo–NiMoO$_x$. (d) Ni K-edge XANES spectra and (e) the corresponding k^2-weighted FT of EXAFS spectra of NiMo–NiMoO$_x$, Ni foil, and NiO. (f) WT plot for the k^2-weighted EXAFS spectra at Ni K-edge of NiMo–NiMoO$_x$. (g) Mo K-edge XANES spectra and (h) the corresponding k^2-weighted FT of EXAFS spectra of NiMo–NiMoO$_x$, Mo foil, and MoO$_3$. (i) WT plot for the k^2-weighted EXAFS spectra at Mo K-edge of NiMo–NiMoO$_x$.

plot for the Ni K-edge of NiMo–NiMoO$_x$ (Fig. 3(f)) shows apparently Ni–Ni/Mo bond, the Ni–O bond is hard to be observed because of its low content. The small WT plots for Ni foil and NiO Ni K-edge are also shown in Fig. S10 in the ESM.

Similarly, the Mo K-edge XANES and EXAFS spectra were also obtained for comprehensive analysis. Figure 3(g) shows that E_0 for Mo in NiMo–NiMoO$_x$ is between that in Mo foil and MoO$_3$, manifesting that Mo atoms are in partially oxidized states. Moreover, the EXAFS spectra (Fig. 3(h)) show the coexistence of the Mo–M (Mo/Ni) and the Mo–O bonds for NiMo–NiMoO$_x$, indicating that Mo atoms exist in both metallic and oxidized states in the sample [52, 53]. The fitting results (Fig. S11 and Table S5 in the ESM) of NiMo–NiMoO$_x$ in *R*-space and *k*-space for Mo further demonstrate the existence of Mo atoms in Ni crystalline and NiO amorphous structure. Compared to Mo foil and MoO$_3$ (Fig. S12 in the ESM), Mo–Ni/Mo bond can be obviously observed, while Mo–O bond is also hard to be see due to the low intensity in the small WT plot for NiMo–NiMoO$_x$ Mo K-edge in Fig. 3(i).

The electrocatalytic HER performance of the NiMo–NiMoO$_x$ catalyst was evaluated in 1 M KOH solution together with NF, Ni–NiO$_x$, and Pt/C. We first investigated the optimal electrodeposition conditions, including time, current density, and Mo source concentration, for preparing the NiMo–NiMoO$_x$ catalyst (Fig. S13 in the ESM). Figures 4(a) and 4(b) show the *iR*-corrected polarization curves and the overpotential at different current densities. As expected, the NiMo–NiMoO$_x$ catalyst exhibits higher activity than the Ni–NiO$_x$ catalyst and even outperforms Pt/C. The synthesized NiMo–NiMoO$_x$ displays an excellent activity, requiring an ultralow overpotential of only 30 mV for 10 mA·cm^{-2} and 142 mV for 200 mA·cm^{-2}, while the Ni–NiO$_x$ catalyst needs 110 and 297 mV, respectively.

Compared to Ni–NiO$_x$, as shown in Fig. 4(c), the Tafel slope of NiMo–NiMoO$_x$ decreases from 102 to 65 mV·dec^{-1} after the introduction of Mo atoms, indicating enhanced HER kinetics and faster electron transfer in NiMo–NiMoO$_x$. Additionally, the Tafel slopes of the two catalysts reveal that the HER process may be controlled by the Volmer–Heyrovsky mechanism. The values of double-layer capacitance (C_{dl}) are proportional to the effective electrochemical active surface area (ECSA) of the solid–liquid interface. As exhibited in Fig. 4(d), the values are measured to be 0.92, 19.48, 19.39, and 12.62 mF·cm^{-2}.

Electrochemical impedance spectroscopy (EIS) was employed to get further insight into the HER electrode dynamics. Figure 4(e) and Table S6 in the ESM show that NiMo–NiMoO$_x$ catalyst obviously possesses the smaller charge transfer resistance (R_{ct}), indicating the faster electron transfer due to the introduction of Mo atoms. The above results demonstrate that the Mo atoms can effectively modulate the electron structure of active site and enhance the electron conductivity, thus boosting the HER activity. The stability of the NiMo–NiMoO$_x$ catalyst was measured at the current density of 10 mA·cm^{-2}. As shown in Fig. 4(f), the voltage varies only about 10 mV after operating for 80 h, exhibiting

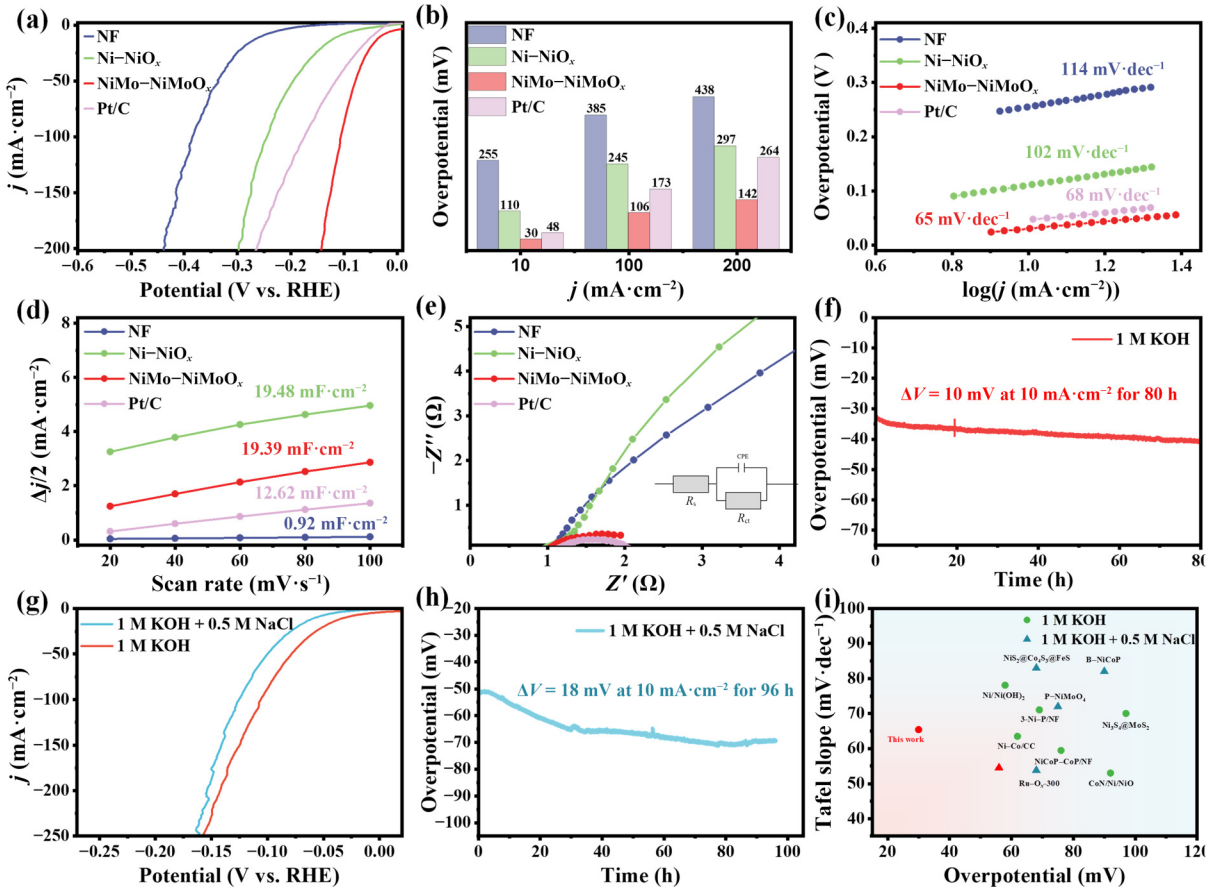

Figure 4 (a) HER polarization curves of NF, commercial Pt/C, Ni–NiO$_x$, and NiMo–NiMoO$_x$ in 1 M KOH. (b) Overpotentials at the current density of 10, 100, and 200 mA·cm^{-2} for the catalysts. (c) Tafel plots, (d) linear fitting of the capacitive current densities vs the scan rates, and (e) EIS Nyquist plots for the catalysts. (f) Stability test for NiMo–NiMoO$_x$ at 10 mA·cm^{-2}. (g) HER linear sweep voltammetry (LSV) curves and (h) stability tested in simulated alkaline seawater. (i) Comparison of the overpotential at 10 mA·cm^{-2} for HER in 1 M KOH and alkaline seawater.

excellent stability in alkaline solution. However, we found that some flakes peeled off from the surface, and the intensity of Mo in XPS spectra decreased, contributing to the deteriorated electrode performance (Figs. S14 and S15 in the ESM). Compared with state-of-the-art HER electrocatalysts (Fig. 4(i) and Table S7 in the ESM), the HER performance of NiMo–NiMoO$_x$ is superior to most reported catalysts.

Seawater electrolysis has attracted growing interest due to the abundant resource reserves and the great promise for industrial hydrogen production without exacerbating freshwater shortages. Given the above considerations, NiMo–NiMoO$_x$ was tested in the simulated alkaline seawater containing 1 M KOH and 0.5 M NaCl. From Fig. 4(g), the HER performance decreased slightly. NiMo–NiMoO$_x$ require 57 and 154 mV to deliver the current density of 10 and 200 mA·cm^{-2}. Besides, the NiMo–NiMoO$_x$ catalyst also possessed favorable stability in the simulated seawater. The voltage changed about 18 mV for almost 100 h (Fig. 4(h)). The Faradaic efficiency (FE) is often used to evaluate the energy efficiency of the catalysts and device. Figure S16 in the ESM shows the volume changes of hydrogen and oxygen produced at 50 mA·cm^{-2} for 40 min. The volume ratio of hydrogen to oxygen is near 2:1, and the calculated FE of hydrogen reaches almost 100%.

Additionally, we also investigated the stability of NiMo–NiMoO$_x$ and Ni–NiO$_x$ in real seawater. As shown in Fig. S17, NiMo–NiMoO$_x$ exhibits excellent stability in real seawater, while the overpotential of Ni–NiO$_x$ decreases by over 150 mV, demonstrating that the introduction of Mo atoms can greatly improve the electrocatalytic performance. This can be attributed to the following mechanisms according to relevant Refs. [54, 55]: During the electrochemical process, Mo atoms gradually dissolve and are released onto the electrode surface in the form of MoO_4^{2-}. Subsequently, MoO_4^{2-} adsorbs on active sites and reduces the surface concentration of Cl^- through electrostatic repulsion. Besides, MoO_4^{2-} can modulate the electronic structure of the catalyst, thereby enhancing stability in Cl^--containing environments.

DFT calculations were performed for understanding the fundamental mechanism of the crystalline-amorphous NiMo–NiMoO$_x$ catalyst at the theoretical level. Based on the experimental results and previous literature, the Volmer–Heyrovsky pathway is adopted for the HER process according to the Tafel slope (Fig. S18 in the ESM) [56, 57].

As shown in Fig. 5(a), the charge density difference plot at the interface of NiMo–NiMoO$_x$ clearly reveals the electron accumulation around Ni atoms and electron depletion around Mo atoms, resulting in the charge redistribution and the optimized electronic structure, which leads to efficient hydrogen evolution [58, 59]. Additionally, the charge-density differences result of Ni–NiO$_x$ is shown in Fig. S19 in the ESM. Compared with NiMo–NiMoO$_x$, Ni atoms near Mo atoms in Ni–NiO$_x$ have fewer electrons, further demonstrating that the introduction of Mo atoms can modulate the charge redistribution in the interface.

Besides, we also compared the difference between the total

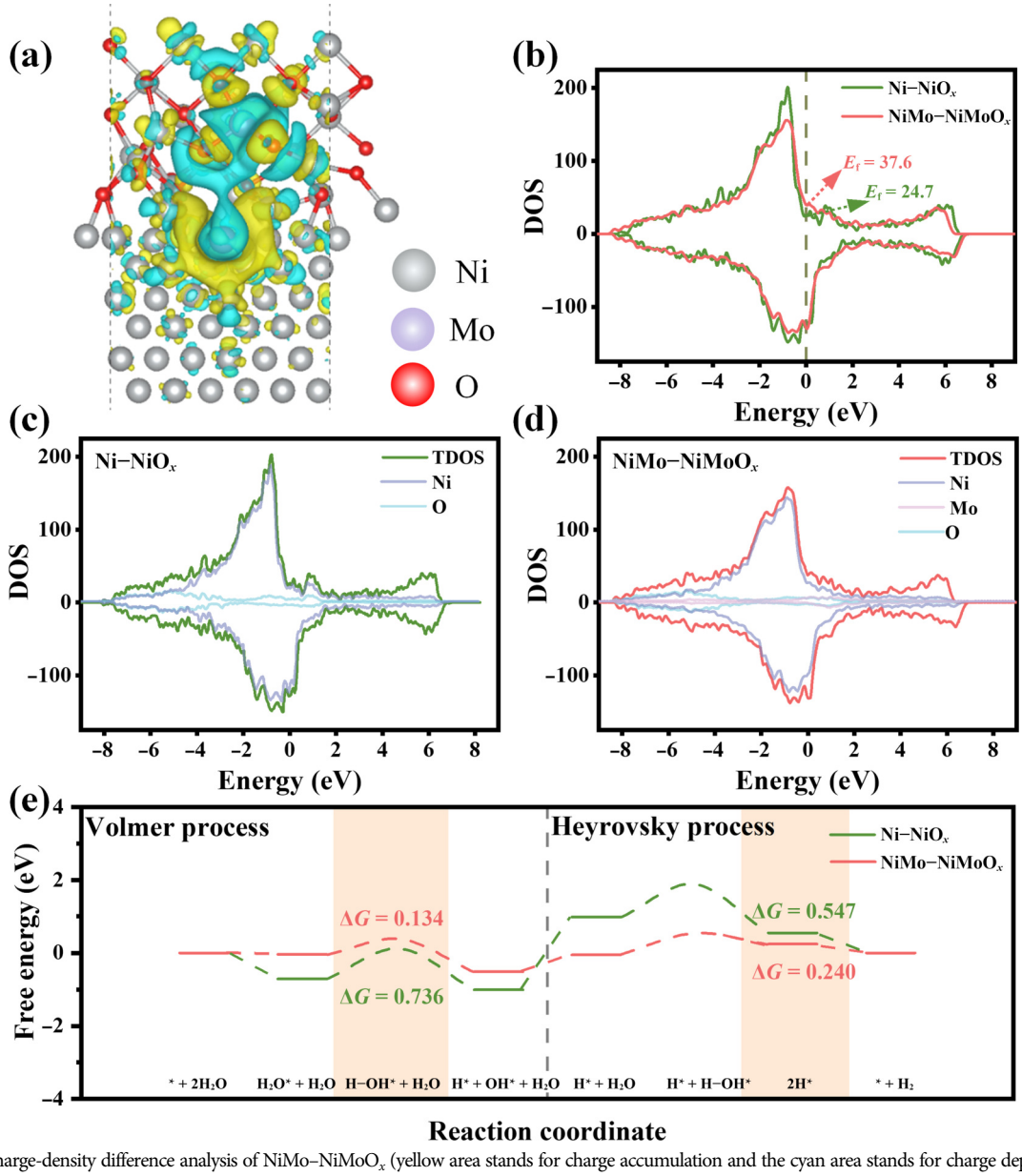

Figure 5 (a) Charge-density difference analysis of NiMo–NiMoO$_x$ (yellow area stands for charge accumulation and the cyan area stands for charge depletion). (b) DOS plots of Ni–NiO$_x$ and NiMo–NiMoO$_x$. (c) DOS plots of Ni–NiO$_x$. (d) DOS plots of NiMo–NiMoO$_x$. (e) Reaction energy diagram of Ni–NiO$_x$ and NiMo–NiMoO$_x$ for HER.

density of states (TDOS) plots of Ni–NiO$_x$ and NiMo–NiMoO$_x$. As shown in Fig. 5(b), the NiMo–NiMoO$_x$ exhibits increased DOS than Ni–NiO$_x$ at the Fermi level without an evident gap. This indicates that there are more free electrons and metallic property with improved electrical conductivity after the introduction of Mo atoms, which enhances the activity of the catalyst. Moreover, the introduction of Mo atoms shifts the d-band center from −1.363 to −1.347 eV, which is closer to the Fermi level. It indicates that the Mo atoms can balance the adsorption and desorption strength of the intermediates and decrease the energy barrier for the dissociation of water [60, 61]. In addition, the projected DOS (PDOS) plots for Ni–NiO$_x$ and NiMo–NiMoO$_x$ (Figs. 5(c) and 5(d)) clearly demonstrate that Mo atoms significantly enhance the DOS and modulate the electronic structure. Figure 5(e) illustrates the reaction pathways and the free energy changes for HER. Though water molecules prefer to adsorb on the Ni–NiO$_x$, the free energy for water dissociation on NiMo–NiMoO$_x$ is smaller, greatly accelerating the Volmer step. Besides, the free energy of H adsorption is also a crucial criterion to identify the activity for HER. We calculated the free energy of H* through the Heyrovsky step (H* + H$_2$O + e$^-$ → H$_2$), and the results show that the ΔG_{H^*} for the NiMo–NiMoO$_x$ is closer to zero, indicating enhanced activity for HER. These calculations demonstrate the Mo atoms play an important role in the enhanced HER performance.

4 Conclusions

In summary, the NiMo–NiMoO$_x$ crystalline-amorphous heterostructure has been successfully grown on Ni foam via a facile one-step electrodeposition process. The introduction of Mo atoms effectively modulates the proportion of the crystalline and amorphous phases, increasing the interfaces between the crystalline

and amorphous phases. Moreover, Mo atoms can lower the energy barrier for water dissociation, optimize the hydrogen adsorption capacity (H_{ad}), and accelerate the kinetics of HER. The NiMo–NiMoO$_x$ catalyst exhibits excellent electrocatalytic activity and stability for alkaline and simulated seawater. It requires only 30 mV overpotential to deliver the current density of 10 mA·cm^{-2} and can operate for 80 h with slight decay. Besides, it also exhibits remarkable stability for 96 h with an overpotential increase of only 18 mV in alkaline simulated seawater. Such excellent performance could be attributed to the synergistic effect of the crystalline and amorphous heterostructure. This study also shows a novel strategy to modulate the interface in the crystalline-amorphous heterostructures.

Electronic Supplementary Material: Supplementary material (further details of electrochemical measurement, DFT calculations, and other characterization results) is available in the online version of this article at https://doi.org/10.26599/NR.2025.94907368.

Data availability

All data needed to support the conclusions in the paper are presented in the manuscript and the Electronic Supplementary Material. Additional data related to this paper may be requested from the corresponding author upon request.

Acknowledgements

This work was financially supported by the National Natural Science Foundation of China (No. 52274294) and the Liaoning Province Science and Technology Plan Joint Program (Key Research and Development Program Project, No. 2023JH2/101800058).

Declaration of competing interest

All the contributing authors report no conflict of interests in this work.

Author contribution statement

X. J. T.: Data curation, validation, writing manuscript, experimental design. Z. W.: Data curation, experimental design. J. Q. L.: Data curation, experimental design, writing manuscript. J. S. Y.: Data curation, writing manuscript. Q. W.: Project administration, funding acquisition. S. Y.: Project administration, funding acquisition. All the authors have approved the final manuscript.

Use of AI statement

None.

References

[1] Wan, Y. J.; Chen, W. B.; Wu, S. Q.; Gao, S.; Xiong, F.; Guo, W. H.; Feng, L.; Cai, K. T.; Zheng, L. R.; Wang, Y. G. et al. Confinement engineering of zinc single-atom triggered charge redistribution on ruthenium site for alkaline hydrogen production. *Adv. Mater.* **2024**, *36*, 2308798.

[2] Qi, S.; Liao, J. L.; Chen, K. Z.; Li, S. K.; Zhao, J. W.; Huang, T. C.; Meng, N.; Yang, H. P.; Hu, Q.; He, C. X. Constructing hierarchical arrays with core–shell metal oxides@metal coordination polymers for efficient and stable overall water splitting. *Nano Res.* **2024**, *17*, 4882–4888.

[3] Mariappan, V. K.; Krishnamoorthy, K.; Pazhamalai, P.; Swaminathan, R.; Kim, S. J. Stimulus of work function on electron transfer process of intermetallic nickel–antimonide toward bifunctional electrocatalyst for overall water splitting. *Small* **2024**, *20*, 2402355.

[4] Wang, Z.; Tan, X. J.; Ye, Z. Y.; Chen, S. Y.; Li, G. J.; Wang, Q.; Yuan, S. High entropy materials: Potential catalysts for electrochemical water splitting. *Green Chem.* **2024**, *26*, 9569–9598.

[5] Li, L. L.; Yu, D. S.; Li, P.; Huang, H. J.; Xie, D. Y.; Lin, C. C.; Hu, F.; Chen, H. Y.; Peng, S. J. Interfacial electronic coupling of ultrathin transition-metal hydroxide nanosheets with layered MXenes as a new prototype for platinum-like hydrogen evolution. *Energy Environ. Sci.* **2021**, *14*, 6419–6427.

[6] Luo, M.; Yang, J. T.; Li, X. G.; Eguchi, M.; Yamauchi, Y.; Wang, Z. L. Insights into alloy/oxide or hydroxide interfaces in Ni–Mo-based electrocatalysts for hydrogen evolution under alkaline conditions. *Chem. Sci.* **2023**, *14*, 3400–3414.

[7] Tan, Y. Y.; Zhang, Z. Y.; Wu, W.; Chen, S. H.; Chen, W.; Cheng, N. C. Breaking Volmer step limitation on NiO/PtNi heterojunctions via ATO-induced charge injection and interfacial modulation. *Appl. Catal. B: Environ.* **2023**, *331*, 122684.

[8] Wang, X. D.; Fang, J. J.; Liu, X. R.; Wei, D.; Yin, Y. Q.; Wei, H. L.; Zhang, J. L.; Zhang, Y. F.; Zhang, X. J.; Zhu, W. et al. Nitrogen-doped carbon as selectively permeable layer to enhance the anti-poisoning ability of hydrogen oxidation reaction catalysts for hydroxide exchange membrane fuel cells. *Appl. Catal. B: Environ.* **2023**, *327*, 122442.

[9] Liang, Q. R.; Li, Q. Z.; Xie, L.; Zeng, H.; Zhou, S.; Huang, Y. N.; Yan, M.; Zhang, X.; Liu, T. Y.; Zeng, J. et al. Superassembly of surface-enriched Ru nanoclusters from trapping-bonding strategy for efficient hydrogen evolution. *ACS Nano* **2022**, *16*, 7993–8004.

[10] Zeng, L. Y.; Zhao, Z. L.; Lv, F.; Xia, Z. H.; Lu, S. Y.; Li, J.; Sun, K. A.; Wang, K.; Sun, Y. J.; Huang, Q. Z. et al. Anti-dissolution Pt single site with Pt(OH)(O_3)/Co(P) coordination for efficient alkaline water splitting electrolyzer. *Nat. Commun.* **2022**, *13*, 3822.

[11] Gong, M.; Wang, D. Y.; Chen, C. C.; Hwang, B. J.; Dai, H. J. A mini review on nickel-based electrocatalysts for alkaline hydrogen evolution reaction. *Nano Res.* **2016**, *9*, 28–46.

[12] Jia, H. L.; Wang, H. Y.; Yan, F. F.; Zhang, H. C.; Li, Z.; Wang, J. J. Unravelling electrocatalytic concerted diatomic-ensembles over superior hydrogen-evolution array structured by NiMo/Mo_2N heteronanojunctions. *Appl. Catal. B: Environ.* **2024**, *343*, 123362.

[13] Wang, Z.; Yuan, S.; Tian, H.; Zang, T.; Li, J. Y.; Liu, J. Q.; Li, G. J.; Wang, J.; Liu, T.; Wang, Q. Magnetic field assisted synthesis of dense braided rope NiCoP as a highly efficient hydrogen evolution electrocatalyst. *Appl. Catal. B: Environ.* **2024**, *343*, 123579.

[14] Chen, F.; Peng, W. F.; Zhou, J. S.; Ma, X. Z.; Wang, Y.; Zhang, Y.; Gao, F. M. Ultrastable and highly efficient hydrogen evolution by heterogeneous NiO/Ni catalysts under industrial electrolysis conditions. *Inorg. Chem. Front.* **2024**, *11*, 425–435.

[15] Li, X. P.; Wang, Y.; Wang, J. J.; Da, Y. M.; Zhang, J. F.; Li, L. L.; Zhong, C.; Deng, Y. D.; Han, X. P.; Hu, W. B. Sequential electrodeposition of bifunctional catalytically active structures in MoO_3/Ni–NiO composite electrocatalysts for selective hydrogen and oxygen evolution. *Adv. Mater.* **2020**, *32*, 2003414.

[16] Yuan, Z. B.; Yao, X.; Zhang, G. G.; Fu, N. Q.; Liu, Y.; Ye, F. Regulating the heterostructure of metal/oxide toward the enhanced hydrogen evolution reaction. *ACS Appl. Energy Mater.* **2022**, *5*, 5644–5651.

[17] Zhao, L.; Zhang, Y.; Zhao, Z. L.; Zhang, Q. H.; Huang, L. B.; Gu, L.; Lu, G.; Hu, J. S.; Wan, L. J. Steering elementary steps towards efficient alkaline hydrogen evolution via size-dependent Ni/NiO nanoscale heterosurfaces. *Natl. Sci. Rev.* **2020**, *7*, 27–36.

[18] Yan, Y. Q.; Ma, Q. H.; Cui, F.; Zhang, J. J.; Cui, T. Y. Carbon onions coated Ni/NiO nanoparticles as catalysts for alkaline hydrogen evolution reaction. *Electrochim. Acta.* **2022**, *430*, 141090.

[19] Dong, Z. H.; Lin, F.; Yao, Y. H.; Jiao, L. F. Crystalline $Ni(OH)_2$/amorphous $NiMoO_x$ mixed-catalyst with Pt-like performance for hydrogen production. *Adv. Energy Mater.* **2019**, *9*, 1902703.
[20] Sun, P. L.; Zheng, X.; Chen, A. R.; Zheng, G. H.; Wu, Y.; Long, M.; Zhang, Q. R.; Chen, Y. G. Constructing amorphous-crystalline interfacial bifunctional site island-sea synergy by morphology engineering boosts alkaline seawater hydrogen evolution. *Adv. Sci.* **2024**, *24*, 2309927.
[21] Singh, T. I.; Maibam, A.; Cha, D. C.; Yoo, S.; Babarao, R.; Lee, S. U.; Lee, S. High-alkaline water-splitting activity of mesoporous 3D heterostructures: An amorphous-shell@crystalline-core nano-assembly of Co–Ni-phosphate ultrathin-nanosheets and V-doped cobalt–nitride nanowires. *Adv. Sci.* **2022**, *9*, 2201311.
[22] Wu, D. L.; Liu, B.; Li, R. D.; Chen, D.; Zeng, W. H.; Zhao, H. Y.; Yao, Y. T.; Qin, R.; Yu, J.; Chen, L. et al. Fe-regulated amorphous-crystal $Ni(Fe)P_2$ nanosheets coupled with Ru powerfully drive seawater splitting at large current density. *Small* **2023**, *19*, 2300030.
[23] Yang, M. Y.; Zhao, M. X.; Yuan, J.; Luo, J. X.; Zhang, J. J.; Lu, Z. G.; Chen, D. Z.; Fu, X. Z.; Wang, L.; Liu, C. Oxygen vacancies and interface engineering on amorphous/crystalline CrO_x–Ni_3N heterostructures toward high-durability and kinetically accelerated water splitting. *Small* **2022**, *18*, 2106554.
[24] Zheng, K. T.; Ren, J. P.; Li, X. M.; Li, G. N.; Jiao, L.; Xu, C. J. Engineering crystalline CoMP-decorated (M = Mn, Fe, Ni, Cu, Zn) amorphous CoM LDH for high-rate alkaline water splitting. *Chem. Eng. J.* **2022**, *441*, 136031.
[25] Wang, Y.; Li, X. P.; Huang, Z.; Wang, H. Z.; Chen, Z. L.; Zhang, J. F.; Zheng, X. R.; Deng, Y. D.; Hu, W. B. Amorphous Mo-doped $NiS_{0.5}Se_{0.5}$ nanosheets@crystalline $NiS_{0.5}Se_{0.5}$ nanorods for high current-density electrocatalytic water splitting in neutral media. *Angew. Chem., Int. Ed.* **2023**, *62*, e202215256.
[26] Xing, M. H.; Zhu, S. K.; Zeng, X. F.; Wang, S. T.; Liu, Z. P.; Cao, D. P. Amorphous/crystalline $Rh(OH)_3$/CoP heterostructure with hydrophilicity/aerophobicity feature for all-pH hydrogen evolution reactions. *Adv. Energy Mater.* **2023**, *13*, 2302376.
[27] Zhong, B.; Wan, S. J.; Kuang, P. Y.; Cheng, B.; Yu, L.; Yu, J. G. Crystalline/amorphous Ni/Ni_xS_y supported on hierarchical porous nickel foam for high-current-density hydrogen evolution. *Appl. Catal. B: Environ.* **2024**, *340*, 123195.
[28] Kang, Y. Q.; Jiang, B.; Malgras, V.; Guo, Y. N.; Cretu, O.; Kimoto, K.; Ashok, A.; Wan, Z.; Li, H. X.; Sugahara, Y. et al. Heterostructuring mesoporous 2D iridium nanosheets with amorphous nickel boron oxide layers to improve electrolytic water splitting. *Small Methods.* **2021**, *5*, 2100679.
[29] Zhang, F.; Zhao, R.; Wang, Y. R.; Han, L.; Gu, J. M.; Niu, Z. M.; Yuan, Y. M.; Qu, N. R.; Meng, J. X.; Wang, D. S. Superwettable surface-dependent efficiently electrocatalytic water splitting based on their excellent liquid adsorption and gas desorption. *Chem. Eng. J.* **2023**, *452*, 139513.
[30] Fan, J. Y.; Zhang, X. Y.; Han, M.; Xiang, X.; Guo, C.; Lin, Y.; Shi, N. E.; Xu, D. D.; Lai, Y.; Bao, J. C. Amorphous Ni–Fe–Mo oxides coupled with crystalline metallic domains for enhanced electrocatalytic oxygen evolution by promoted lattice-oxygen participation. *Small* **2024**, *20*, 2303927.
[31] Gu, Z. X.; Zhang, Y. C.; Wei, X. L.; Duan, Z. Y.; Ren, L.; Ji, J. C.; Zhang, X. Q.; Zhang, Y. X.; Gong, Q. Y.; Wu, H. et al. Unveiling the accelerated water electrolysis kinetics of heterostructural iron–cobalt–nickel sulfides by probing into crystalline/amorphous interfaces in stepwise catalytic reactions. *Adv. Sci.* **2022**, *9*, 2201903.
[32] Liu, X. J.; Liu, R.; Wang, J. M.; Liu, Y. R.; Li, L. H.; Yang, W. X.; Feng, X.; Wang, B. Synergizing high valence metal sites and amorphous/crystalline interfaces in electrochemical reconstructed CoFeOOH heterostructure enables efficient oxygen evolution reaction. *Nano Res.* **2022**, *15*, 8857–8864.
[33] Gojgić, J. D.; Petričevič, A. M.; Rauscher, T.; Bernäcker, C. I.; Weißgärber, T.; Pavko, L.; Vasilić, R.; Pajić, M. N. K.; Jović, V. D. Hydrogen evolution at Ni foam electrodes and Ni–Sn coated Ni foam electrodes. *Appl Catal A: Gen.* **2023**, *663*, 119312.
[34] Wang, X. M.; Long, G. F.; Liu, B.; Li, Z. L.; Gao, W. S.; Zhang, P. F.; Zhang, H.; Zhou, X.; Duan, R. Z.; Hu, W. et al. Rationally modulating the functions of Ni_3Sn_2–$NiSnO_x$ nanocomposite electrocatalysts towards enhanced hydrogen evolution reaction. *Angew. Chem., Int. Ed.* **2023**, *62*, e202301562.
[35] Kim, H.; Kim, J.; Han, G. H.; Guo, W. W.; Hong, S.; Park, J.; Ahn, S. H. Electrodeposited rhenium–cobalt alloy with high activity for acidic hydrogen evolution reaction. *J. Ind. Eng. Chem.* **2021**, *95*, 357–366.
[36] Liu, G. Q.; Bao, A. Y.; Li, C. C.; Zhou, N. N.; Yang, C. Z.; Chen, X.; Li, Y. T.; Liu, D. M. Metallic nickel anchored on amorphous nickel cobalt oxide nanorods as efficient electrocatalysts toward oxygen evolution reaction. *J. Alloys Compd.* **2023**, *947*, 169657.
[37] Gong, Z. C.; Liu, R.; Gong, H. S.; Ye, G. L.; Liu, J. J.; Dong, J. C.; Liao, J. W.; Yan, M. M.; Liu, J. B.; Huang, K. et al. Constructing a graphene-encapsulated amorphous/crystalline heterophase NiFe alloy by microwave thermal shock for boosting the oxygen evolution reaction. *ACS Catal.* **2021**, *11*, 12284–12292.
[38] Liu, T. T.; Gao, W. B.; Wang, Q. Q.; Dou, M. L.; Zhang, Z. P.; Wang, F. Selective loading of atomic platinum on a $RuCeO_x$ support enables stable hydrogen evolution at high current densities. *Angew. Chem., Int. Ed.* **2020**, *59*, 20423–20427.
[39] Deng, L. M.; Hung, S. F.; Zhao, S.; Zeng, W. J.; Lin, Z. Y.; Hu, F.; Xie, Y. Y.; Yin, L. J.; Li, L. L.; Peng, S. J. Unveiling coordination transformation for dynamically enhanced hydrogen evolution catalysis. *Energy Environ. Sci.* **2023**, *16*, 5220–5230.
[40] Xu, R.; Wu, R.; Shi, Y. M.; Zhang, J. F.; Zhang, B. Ni_3Se_2 nanoforest/Ni foam as a hydrophilic, metallic, and self-supported bifunctional electrocatalyst for both H_2 and O_2 generations. *Nano Energy* **2016**, *24*, 103–110.
[41] Luo, Y. T.; Zhang, Z. Y.; Yang, F. N.; Li, J.; Liu, Z. B.; Ren, W. C.; Zhang, S.; Liu, B. L. Stabilized hydroxide-mediated nickel-based electrocatalysts for high-current-density hydrogen evolution in alkaline media. *Energy Environ. Sci.* **2021**, *14*, 4610–4619.
[42] Zhou, N. N.; Hu, H.; Chai, X. L.; Liu, R.; Pei, Z. B.; Liang, S.; Hu, L.; Yang, L.; Hu, K. H.; Huang, Z. L. et al. Synergistic heterointerface engineering of Co_9S_8/$Ni(OH)_2$ hierarchical nanosheets for remarkable overall water splitting. *Int. J. Hydrogen Energy* **2024**, *63*, 114–122.
[43] Singu, B. S.; Chitumalla, R. K.; Mandal, D.; Kim, Y.; Kim, G. H.; Chung, H. T.; Jang, J.; Kim, H. Development of metal–organic framework-derived NiMo–MoO_{3-x} porous nanorod for efficient electrocatalytic hydrogen evolution reactions. *Appl. Catal. B: Environ.* **2023**, *328*, 122421.
[44] Yuan, W. J.; Cui, Z. D.; Zhu, S. L.; Li, Z. Y.; Wu, S. L.; Liang, Y. Q. Structure engineering of electrodeposited NiMo films for highly efficient and durable seawater splitting. *Electrochim. Acta.* **2021**, *365*, 137366.
[45] Zhang, J. Y.; Zhang, S. S.; Zhang, X. F.; Ma, Z.; Wang, Z.; Zhao, B. Construction of Ni_4Mo/MoO_2 heterostructure on oxygen vacancy enriched $NiMoO_4$ nanorods as an efficient bifunctional electrocatalyst for overall water splitting. *J. Colloid Interface Sci.* **2023**, *650*, 1490–1499.
[46] Li, J. X.; Lv, Y.; Wu, X. Y.; Zhao, K. N.; Guo, J. X.; He, B. H.; Jia, D. Z. Iron doping and interface engineering on amorphous/crystalline Fe–Ni_xS_y heterostructures toward high-stability and kinetically accelerated water splitting. *J. Colloid Interface Sci.* **2023**, *650*, 1086–1096.
[47] Park, J.; Kim, H.; Han, G. H.; Kim, J.; Yoo, S. J.; Kim, H. J.; Ahn, S. H. Electrochemically fabricated MoO_3–MoO_2@NiMo heterostructure catalyst with Pt-like activity for the pH-universal hydrogen evolution reaction. *J. Mater. Chem. A* **2021**, *9*, 3677–3684.
[48] Li, Q.; Chen, C.; Luo, W. S.; Yu, X.; Chang, Z. W.; Kong, F. T.; Zhu, L. B.; Huang, Y. F.; Tian, H.; Cui, X. Z. et al. *In situ* active site refreshing of electro-catalytic materials for ultra-durable hydrogen evolution at elevated current density. *Adv. Energy Mater.* **2024**, *14*, 2304099.

[49] Xiao, L. Y.; Yang, T. T.; Cheng, C. Q.; Du, X. W.; Zhao, Y.; Liu, Z. W.; Zhao, X. R.; Zhang, J. T.; Zhou, M.; Han, C. Y. et al. Coupled compressive-tensile stains boosting both activity and durability of NiMo electrode for alkaline water/seawater hydrogen evolution at high current densities. *Chem. Eng. J.* **2024**, *485*, 150044.

[50] Wang, M.; Yang, H.; Shi, J. N.; Chen, Y. F.; Zhou, Y.; Wang, L. G.; Di, S. J.; Zhao, X.; Zhong, J.; Cheng, T. et al. Alloying nickel with molybdenum significantly accelerates alkaline hydrogen electrocatalysis. *Angew. Chem., Int. Ed.* **2021**, *60*, 5771–5777.

[51] Zhang, Y. W.; Fan, G. L.; Yang, L.; Zheng, L. R.; Li, F. Cooperative effects between Ni–Mo alloy sites and defective structures over hierarchical Ni–Mo bimetallic catalysts enable the enhanced hydrodeoxygenation activity. *ACS Sustainable Chem. Eng.* **2021**, *9*, 11604–11615.

[52] Chen, Y. H.; Yue, K. H.; Zhao, J. W.; Cai, Z. Y.; Wang, X. Y.; Yan, Y. Effective modulating of the Mo dissolution and polymerization in $Ni_4Mo/NiMoO_4$ heterostructure via metal–metal oxide–support interaction for boosting H_2 production. *Chem. Eng. J.* **2023**, *466*, 143097.

[53] Maji, M.; Dutta, S.; Jena, R.; Dey, A.; Maji, T. K.; Pati, S. K.; Bhattacharyya, S. Hydrogen evolution in neutral media by differential intermediate binding at charge-modulated sites of a bimetallic alloy electrocatalyst. *Angew. Chem., Int. Ed.* **2024**, *63*, e202403697.

[54] Kang, X.; Yang, F. N.; Zhang, Z. Y.; Liu, H. M.; Ge, S. Y.; Hu, S. Q.; Li, S. H.; Luo, Y. T.; Yu, Q. M.; Liu, Z. B. et al. A corrosion-resistant RuMoNi catalyst for efficient and long-lasting seawater oxidation and anion exchange membrane electrolyzer. *Nat. Commun.* **2023**, *14*, 3607.

[55] Du, W.; Shi, Y. M.; Zhou, W.; Yu, Y. F.; Zhang, B. Unveiling the *in situ* dissolution and polymerization of Mo in Ni_4Mo alloy for promoting the hydrogen evolution reaction. *Angew. Chem., Int. Ed.* **2021**, *60*, 7051–7055.

[56] Jin, M. T.; Zhang, X.; Niu, S. Z.; Wang, Q.; Huang, R. Q.; Ling, R. H.; Huang, J. Q.; Shi, R.; Amini, A.; Cheng, C. Strategies for designing high-performance hydrogen evolution reaction electrocatalysts at large current densities above 1000 $mA \cdot cm^{-2}$. *ACS Nano* **2022**, *16*, 11577–11597.

[57] Yi, X. R.; He, X. B.; Yin, F. X.; Li, G. R.; Li, Z. C. Surface strain engineered Ni–NiO for boosting hydrogen evolution reaction in alkaline media. *Electrochim. Acta.* **2021**, *391*, 138985.

[58] Zhang, Y.; Li, K.; Li, Y. K.; Mi, J. B.; Li, C. X.; Li, H. D.; Wang, L. Charge redistribution of lattice-mismatched Co–Cu_3P boosting pH-universal water/seawater hydrogen evolution. *Small* **2024**, *20*, 2400244.

[59] Zhao, Y. F.; Zhang, H.; Chen, J.; Zhao, S. W.; Xi, M.; Yang, L. F.; Long, Y. Y.; Ni, Z. T.; Zhou, Y.; Chen, A. R. Interfacial electronic engineering of heterostructured Co_2P–MoNiP/NF nano-sea-urchin catalysts for efficient and stable hydrogen evolution via water/seawater splitting. *Chem. Eng. J.* **2023**, *477*, 147092.

[60] Li, X. J.; Wu, T. T.; Li, N.; Zhang, S. T.; Chang, W. J.; Chi, J. Q.; Liu, X. B.; Wang, L. Vertically staggered porous Ni_2P/Fe_2P nanosheets with trace Ru doping as bifunctional electrocatalyst for alkaline seawater splitting. *Adv. Funct. Mater.* **2024**, *34*, 2400734.

[61] Wang, X. Y.; Liu, X. B.; Wu, S. Q.; Liu, K.; Meng, X. M.; Li, B.; Lai, J. P.; Wang, L.; Feng, S. H. Phosphorus vacancies enriched cobalt phosphide embedded in nitrogen doped carbon matrix enabling seawater splitting at Ampere-level current density. *Nano Energy* **2023**, *109*, 108292.